Journal of Energy Chemistry 61 (2021) 1–7

Contents lists available at ScienceDirect

Journal of Energy Chemistry

journal homepage: www.elsevier.com/locate/jechem

http://www.journals.elsevier.com/journal-of-energy-chemistry/

Adjusting the Sn_{Zn} defects in $Cu_2ZnSn(S,Se)_4$ absorber layer via Ge^{4+} implanting for efficient kesterite solar cells

Yueqing Deng [a,b], Zhengji Zhou [a,b,*], Xin Zhang [a,b], Lei Cao [a,b], Wenhui Zhou [a,b], Dongxing Kou [a,b], Yafang Qi [a,b], Shengjie Yuan [a,b], Zhi Zheng [b,c], Sixin Wu [a,b,*]

[a] Key Lab for Special Functional Materials, Ministry of Education, National and Local Joint Engineering Research Center for High-Efficiency Display and Lighting Technology, And School of Materials, Henan University, Kaifeng 475004, Henan, China
[b] Collaborative Innovation Centre of Nano Functional Materials and Applications, Henan, China
[c] Key Laboratory for Micro-Nano Energy Storage and Conversion Materials of Henan Province, College of Advanced Materials and Energy, Institute of Surface Micro and Nano Materials, Xuchang University, Xuchang 461000, Henan, China

ARTICLE INFO

Article history:
Received 21 December 2020
Revised 3 February 2021
Accepted 13 February 2021
Available online 10 March 2021

Keywords:
CZTSSe
Defect
Absorber layer
Solar cells
V_{oc}

ABSTRACT

The development of kesterite photovoltaic solar cells has been hindered by large open-circuit voltage (V_{oc}) deficit. Recently, Sn_{Zn} deep point defect and associative defect cluster have been recognized as the main culprit for the V_{oc} losses. Therefore, manipulating the deep-level donor of Sn_{Zn} antisite defects is crucial for breaking through the bottleneck of present $Cu_2ZnSn(S,Se)_4$ (CZTSSe) photovoltaic technology. In this study, the Sn_{Zn} deep traps in CZTSSe absorber layer are suppressed by incorporation of Ge. The energy levels and concentration of Sn_{Zn} defects measured by deep-level transient spectroscopy (DLTS) decrease significantly. In addition, the grain growth of CZTSSe films is also promoted due to Ge implantation, yielding the high quality absorber layer. Consequently, the efficiency of CZTSSe solar cells increases from 9.15% to 11.48%, largely attributed to the 41 mV V_{oc} increment.

1. Introduction

$Cu_2ZnSn(S,Se)_4$ (CZTSSe) solar cell has been considered as an ideal candidate for developing green, low-cost, high efficient and stable photovoltaic device due to the availability of constituent elements and high theoretical conversion efficiency [1–5]. Nevertheless, the key limitation to high efficiency in this technology remains a deficit in the open-circuit voltage (V_{oc}) with respect to the band gap [6–8]. Defects caused deep levels and band-tail states are the key factors for high V_{oc} deficiency [9–11]. As a quaternary semiconducting compound, there are many kinds of defects in the bulk phase of CZTSSe absorbing layer, such as Cu_{Zn}, V_{Cu}, Cu_{Sn} and Sn_{Zn} [12–15]. In order to decrease V_{oc} deficit and ultimately increase the power conversion efficiency (PCE) of kesterite-based solar cells, it is urgent to identify the killer defects in CZTSSe absorbers, and further find an appropriate way to passivate them.

Cu-Zn disorder-related defects were initially considered as the main culprit for large V_{oc} deficit. It was believed that the low formation energy of Cu_{Zn} and Zn_{Cu} resulted in high densities of Cu/Zn antisite defects in CZTSSe polycrystalline materials [16]. And a series of strategy has been employed to mitigate the Cu-Zn disorder, for example, partially substituting Cu^+ with Ag^+ [17–19], as well as replacing Zn^{2+} with Cd^{2+} [20–22]. The improved photovoltaic performance has successfully demonstrated the beneficial effects of cation substitution [23]. However, the point defects of Sn_{Zn} have recently been estimated to be especially detrimental to V_{oc} of CZTSSe solar cells [24,25]. It was reported that Sn_{Zn} antisite defects would not only yield deep-donor states in bandgap of CZTSSe [26,27], but also form defect complexes with abundant Cu_{Zn} defects. Moreover, the consequent defect cluster of [$2Cu_{Zn}$ + Sn_{Zn}] is believed to be the origin of band-tail states [28], which will shrink the bandgap of CZTSSe. Therefore, suppressing the concentration of Sn_{Zn} defects is a critical step toward high efficient CZTSSe photovoltaic device.

Preparation of CZTSSe films with Sn-poor composition is an optional way to reduce the concentration of Sn_{Zn}-based defects, whereas at the same time, the crystalline quality of CZTSSe absorbing layer is seriously destroyed. Substituting Sn with the same

* Corresponding authors.
E-mail addresses: zzj@henu.edu.cn (Z. Zhou), wusixin@henu.edu.cn (S. Wu).

https://doi.org/10.1016/j.jechem.2021.02.011

main group element of Ge is worth trying to suppress Sn_{Zn} defects. Furthermore, previous research demonstrated that introducing Ge into CZTSSe could more easily form large-grain absorber layers [29,30]. In this work, we investigate the effect of incorporation of Ge on the composition, crystalline quality as well as photovoltaic performance of CZTSSe thin film solar cells. The results demonstrated that the crystalline quality of CZTSSe absorber layer was improved by doping with Ge, what's more, the concentration of Sn_{Zn} defect was substantially declined due to the isovalent cation-substitution. Consequently, when the thickness of Ge was 15 nm, the PCE has increased from 9.15% to 11.48%, mainly attributed to the increment of V_{oc} from 450 to 491 mV.

2. Experimental

2.1. Materials

Copper powder (99.9%) was obtained from Macklin Reagent Company (China). Zinc powder (99.9%), tin powder (99%), sulfur powder (99.9%) and selenium powder (99.9%) were purchased from Aladdin Ltd. Cadmium sulfate ($CdSO_4{\cdot}8/3H_2O$, 99%, Aladdin), thiourea (NH_2CSNH_2, 99%, Aladdin), 1,2-ethylenediamine ($H_2NCH_2CH_2NH_2$, 99%, Alfa), 2-ethanedithiol ($HSCH_2CH_2SH$, 98+%, Alfa) and ethanolamine (C_2H_7NO, 99.5%, Aladdin) were used as received. Ammonia solution ($NH_3{\cdot}H_2O$, 25%) was obtained from Tianjin Fuyu Fine Chemical Co., Ltd. Thioglycolic acid ($C_2H_4O_2S$, 98%) was purchased from Acros Organics Company. The Germanium granules were purchased from ZhongNuo Advanced Material Technology Company. The above chemicals were used directly without further purification.

2.2. Deposition of Ge ultrathin films

Ge films were deposited on the molybdenum back contact by thermal evaporation using a TEMD500 evaporator. The thickness of Ge films were indicated by a quartz crystal thickness monitor and set as 10, 15 and 20 nm, respectively. The freshly prepared Ge-coated substrates were placed in the inert gas glove box as soon as possible after taking out from the evaporation chamber.

2.3. Preparation of CZTSSe precursor films

CZTSSe precursor solution was synthesized by dissolving 0.0699 g Cu, 0.0494 g Zn, 0.0859 g Sn, 0.0857 g S and 0.0234 g Se in 5 mL 1,2-ethylenediamine and 0.5 mL 1,2-ethanedithiol. After the mixture was stirred for 1.5 h at 70 °C, 1 mL stabilizer (thioglycolic acid:ethanolamine:ethylene glycol methyl ether = 1:1:2) was added into the mixed solution and stirred for another 0.5 h. Finally, a transparent orange-yellow solution was obtained. CZTSSe precursor films were prepared by spin-coating this mixture in a glove box filled with argon gas and sintering on a hot plate at 330 °C for 3 min to remove the organic solvent. The spin-coating and sintering procedure were repeated for 8 cycles and a targeted thickness of 2 μm was finally achieved.

2.4. Assembling CZTSSe photovoltaic devices

The selenization of as-prepared CZTSSe films was carried out in a rapid thermal processing (RTP) furnace using a graphite box containing selenium particles. The annealing temperature rose up to 550 °C in 60 s and held at this temperature for 15 min with a nitrogen flow of 80 mL/min. Then the CdS buffer layer (60 nm) and ZnO (70 nm)/ITO (200 nm) window layer were subsequently deposited on the CZTSSe absorber layer. Finally, an Ag grid was deposited by thermal evaporation to finish the fabrication of the solar cell.

2.5. Characterizations

The X-ray diffraction (XRD) patterns were taken with a Bruker AXS (D8 Advance). The Raman spectra measurement was performed on a Renishaw inVia Raman microscope system with a 532 nm wavelength excitation laser. The scanning electron microscope (SEM) images were obtained using a Nova Nano SEM 450 field emission scanning electron microscope (FESEM). Depth profiling data were obtained with a TOF-SIMS 5 secondary-ion mass spectrometry (SIMS) workstation (IONTOF GmbH). The external quantum efficiency (EQE) spectra were measured using a Zolix SCS100 QE system. The current density–voltage ($J-V$) curves were recorded using a standard lighting conditions (AM 1.5 illumination, 100 mW/cm^2) with a Keithley 2400 source meter. Electrochemistry impedance spectroscopy (EIS) were conducted with a frequency response analysis (FRA) equipped PGSTAT-30 from Autolab (AUT302N, Metrohm, Switzerland). Deep-level transient spectroscopy (DLTS) were acquired from a FT-1030 HERA DLTS system collocated with a JANIS VPF-800 heat controller. DLTS curves were measured in the range of 150 to 350 K, the pulse width, pulse voltage (V_p) and reverse biased (V_R) were set as 10 ms, −0.2 V and 0.4 V, respectively.

3. Results and discussion

3.1. Structural, compositional and morphological characterization of CZTSSe absorber layer

Fig. 1(a) shows XRD patterns of selenized CZTSSe thin films with different thickness of Ge nanometric layer on the Mo back contact substrates. All samples present a tetragonal crystal structure and no diffraction peak of secondary phase can be observed, which indicate that the CZTSSe films formed a homogeneous alloy material with the structure of kesterite. However, in the enlarged image of CZTSSe (112) diffraction peak (Fig. 1b), a gradual shift toward higher 2θ can be easily detected, which indicates that smaller Ge^{4+} (0.39 Å) [31] ions were incorporated into the lattice sites of Sn^{4+} (0.55 Å) ions in the CZTSSe crystal structure, inducing the contraction of CZTSSe unit cell [32]. Similar results are further revealed by Raman spectra, as shown in Fig. 1(c), the Raman peaks located at 172, 197, 236, and 329 cm^{-1} correspond well with kesterite CZTSSe [33–35], no other impure phase has been detected. In the same way, the slight shift of Raman vibration peak (Fig. 1d) may be resulted from the incorporation of Ge into CZTSSe films.

To explore the chemical elements distribution on the cross section of selenized CZTSSe films, the SIMS depth analysis of CZTSSe devices without and with 15 nm Ge-containing was carried out, which are presented in Fig. 2(a and b), respectively. The elemental depth distribution of Cu, Zn and Sn from both of the selenized CZTSSe films display the same trend, suggesting that incorporation of Ge does not change the crystal structure and homogeneity of CZTSSe films. At the same time, it is clear that an almost uniformly distributed Ge in the selenized CZTSSe films can be observed, indicating that Ge is evenly migrated into the CZTSSe films during the selenized process. The XPS analysis of 15 nm Ge-doped sample (Fig. S1) confirms the chemical states and ratio of Ge in CZTSSe films. According to the previous report [36], the decreasing binding energy of Ge $3d_{5/2}$ and Ge $3d_{3/2}$ located at 25.23 and 26.21 eV is possibly because Ge partly occupied the Sn position in CZTSSe lattice. By the quantitative analysis of XPS spectrum, the atomic ratio of Ge/Sn + Ge is 0.75% in the 15 nm Ge-doped CZTSSe absorber layer.

To better understand the effect of Ge-doping on morphology of CZTSSe absorber layer, FESEM measurements were performed on

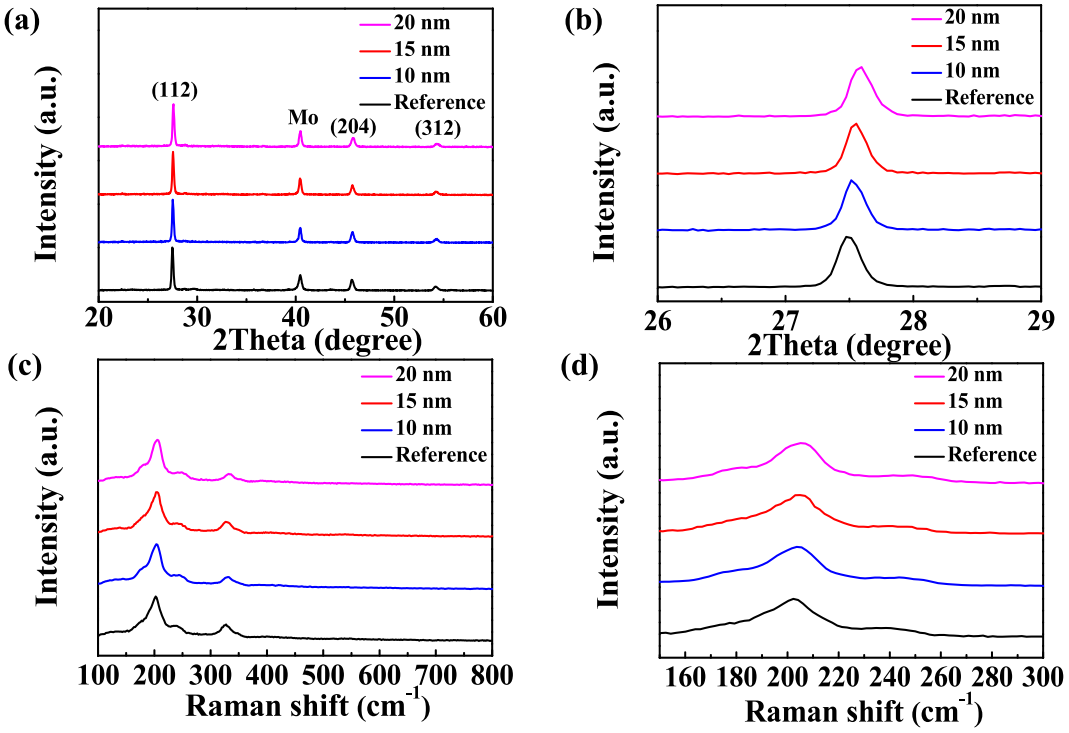

Fig. 1. (a) X-ray diffraction spectra of CZTSSe with different Ge contents. (b) The XRD pattern of main (112) kesterite type structure peak. (c and d) Raman spectra of CZTSSe with different Ge contents.

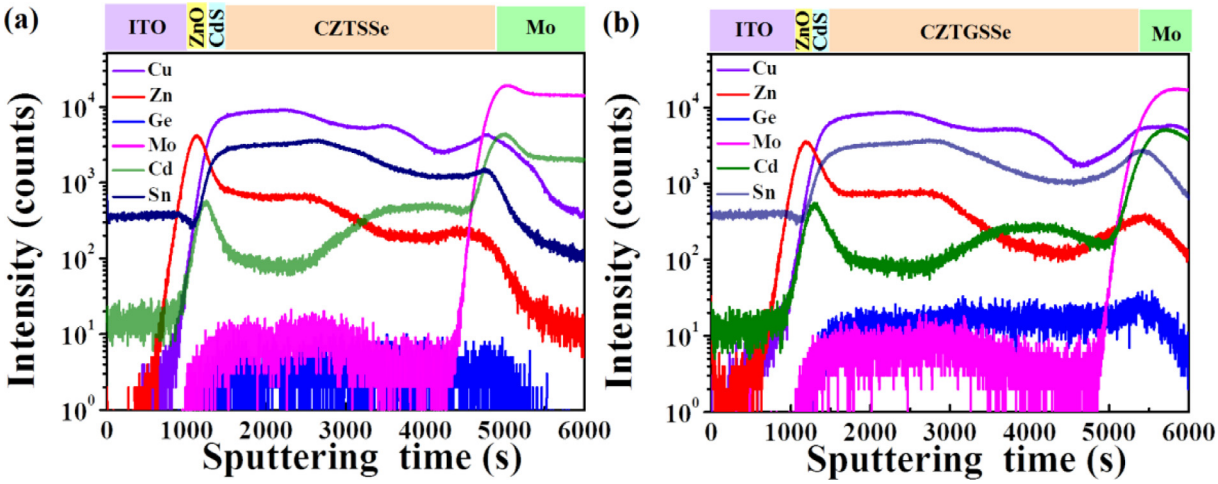

Fig. 2. Secondary ion mass spectroscopy (SIMS) depth profiles of Reference (a) and 15 nm Ge devices (b).

the above two samples. From the cross-sectional FESEM images of the completed CZTSSe solar cells, as shown in Fig. 3(a and b), the thickness of CZTSSe layers are about 2 μm, and both of the absorber layers exhibit a double-layer structure with large grain at top and small grain at bottom, which is consistent with the previous reports [37,38]. However, after the incorporation of Ge, it is evident that the top large-grain layer becomes thicker, and meanwhile the thickness of bottom small-grain layer is obviously reduced, compared with pure CZTSSe film. The change of morphology demonstrates that the quality of CZTSSe absorber layer is significantly improved by doping with Ge. This is consistent with previous reports that Ge doping could promote the grain growth of CZTSSe films, resulting in increasing grain size and photovoltaic efficiency [29,30].

3.2. Characterization of the photovoltaic performance of CZTSSe solar cells

The statistical box charts of photovoltaic parameters as a function of Ge thickness from 18 CZTSSe solar cells are compared in Fig. 4. The average PCE is found to be gradually improved with the thickness of Ge increasing from 0 to 15 nm, which mainly results from the enhancement of open circuit voltage (V_{oc}) and fill factor (FF). When 20 nm Ge was introduced into the CZTSSe solar cells, photovoltaic performance of the devices begins to drop. The illuminated (AM 1.5) current–voltage ($J - V$) measurement results for the champion CZTSSe solar cells with varied thickness of Ge incorporation are presented in Fig. 5(a), and the detailed device parameters are listed in Table 1. When the thickness of Ge is

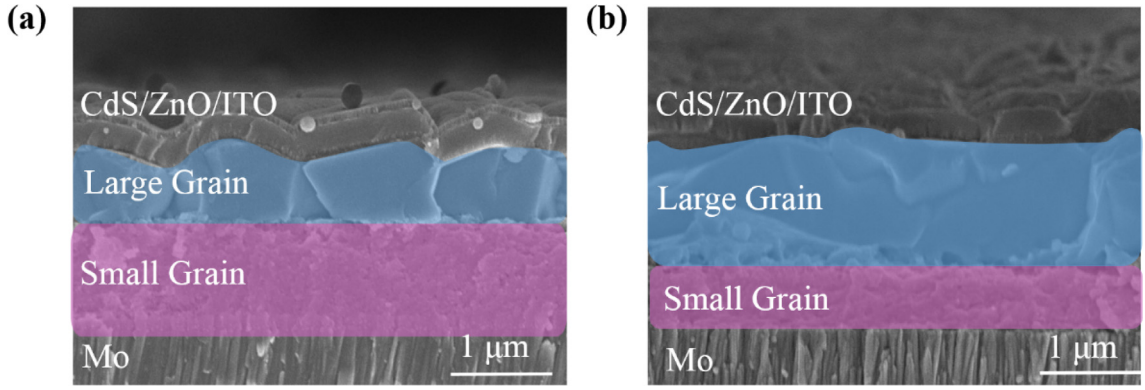

Fig. 3. The cross-sectional SEM images of reference (a) and 15 nm Ge samples (b).

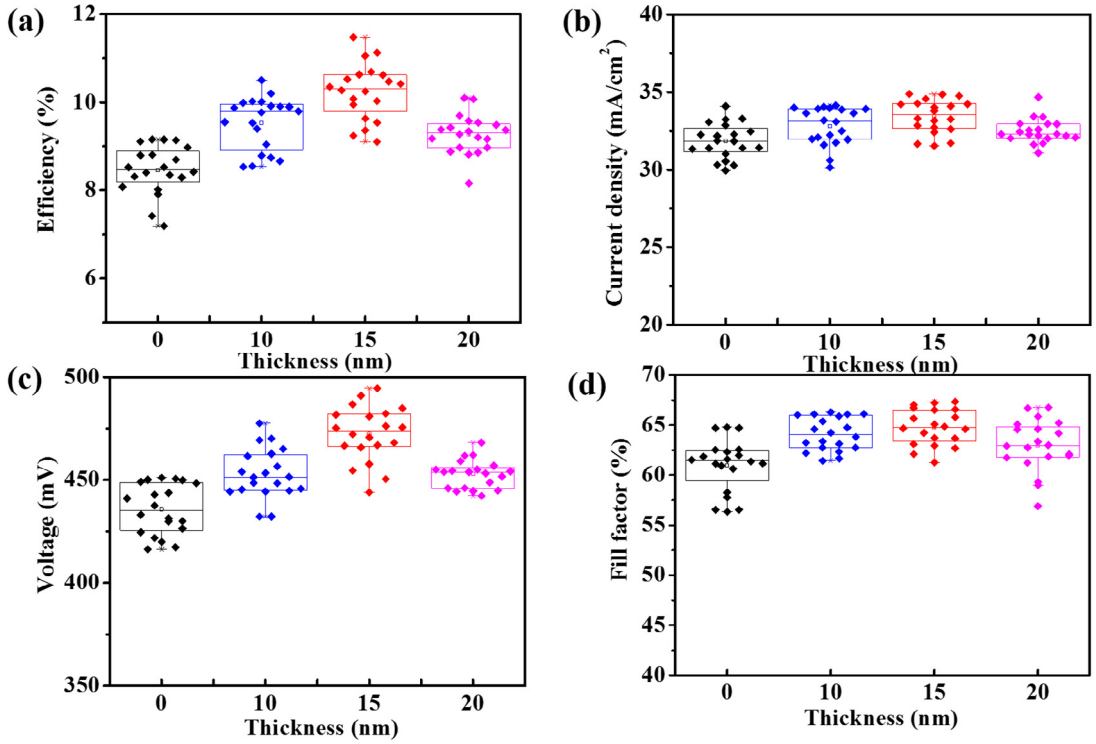

Fig. 4. Statistical box diagrams of performance parameters derived from 18 devices: (a) PCE, (b) J_{sc}, (c) V_{oc} and (d) FF.

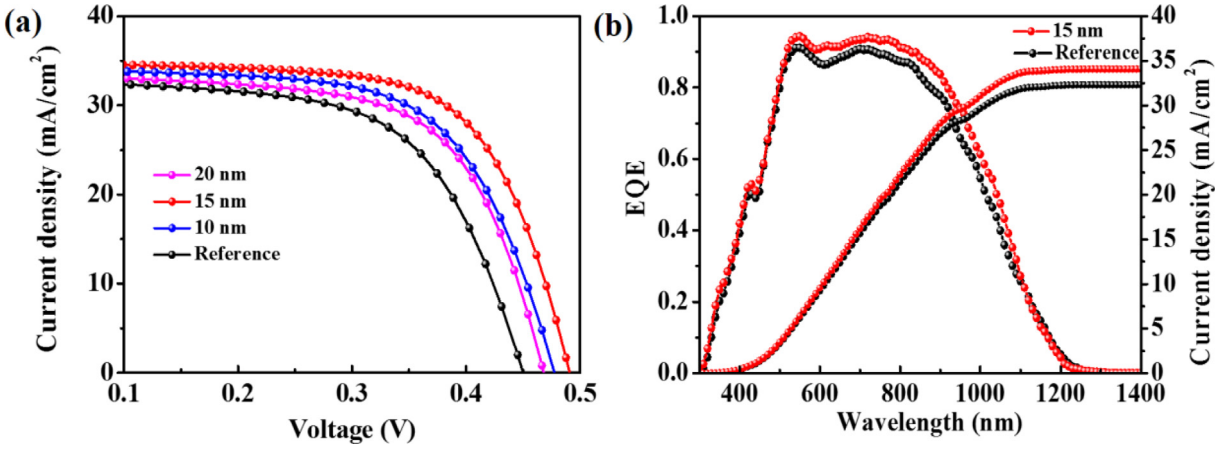

Fig. 5. (a) *J-V* curves of device with different Ge contents. (b) External quantum efficiency curves and integrated J_{sc} of the reference and 15 nm Ge solar cells.

Table 1
The detailed photovoltaic parameters of devices for different thickness of Ge nanolayers.

Device	PCE (%)	J_{sc} (mA/cm^2)	V_{oc} (mV)	FF (%)	R_s (Ω cm^2)	R_{sh} (Ω cm^2)	A	J_0 (mA/cm^2)
Reference	9.15	32.87	450	61.86	1.05	523.56	1.81	1.5×10^{-3}
10 nm	10.50	34.04	477	64.59	0.84	662.25	1.75	6.8×10^{-4}
15 nm	11.48	34.77	491	67.23	0.63	714.29	1.64	2.3×10^{-4}
20 nm	10.11	33.40	468	64.60	0.66	555.56	1.79	8.2×10^{-4}

15 nm, the PCE of CZTSSe devices increase to 11.48%, comparing with 9.15% for the referencing sample, yielding the best photovoltaic performance with a short-circuit current density (J_{sc}) of 34.77 mA/cm^2, a V_{oc} of 491 mV and a FF of 67.23%. In addition, the diode ideal factor (A) and reverse saturation (J_0) current are determined by fitting the $J-V$ curves, as shown in Figs. S2 and S3. It is obvious that the 15 nm Ge device demonstrates the lowest A and J_0 values, indicating the best quality of p-n junction. Whereas the thickness of Ge increases to 20 nm, the values of A and J_0 increase, suggesting that the quality of the p–n junction is decreased, which results in the increase of interface recombination and deterioration of the device performance.

To confirm the improvement of photovoltaic performance, EQE measurement was further carried out. The champion CZTSSe solar cells based on 15 nm Ge-containing and without Ge were chosen in order to compare. The results are displayed in Fig. 5(b), from which we can see that the current densities estimated by integrating the area of the EQE curves are well consistent with the J–V results. Furthermore, it is noticeable that although both of photovoltaic devices show comparable quantum efficiency in the short wavelength (350–500 nm) region, an enhanced quantum efficiency in the visible and near infrared range of 500–1100 nm can be observed for device incorporated with 15 nm Ge. As well known, the enhancement of EQE in longer wavelength demonstrates that the collection of charge carriers in the neutral region is improved [39,40], which can be explained by the decrease of recombination in the bulk of CZTSSe film after Ge doping. These results are well consistent with previous studies [41].

3.3. The mechanism for the improvement of photovoltaic performance

Deep-level defects in the bulk of CZTSSe have been considered as the main origin for the large open circuit voltage deficit [42,43], which will not only form carrier trapping center resulting in nonradiative recombination [44], but also correlate with band tailing causing bandgap fluctuation of CZTSSe absorber layer [45]. The capacitance-mode deep-level transient spectroscopy (C-DLTS) was conducted to evaluate the intrinsic lattice defects after the incorporation of Ge. DLTS measurements were carried out in the temperature range from 150 to 350 K, as shown in Fig. 6(a), an obvious peak around 300 K is observed in both samples, indicating a deep energy level is detected. The trap activation energy (E_a) and density (N_T) of the defect can be extracted from the Arrhenius plot by linear fitting of the points around the peak in DLTS, and the results are displayed in Fig. 6(b) and Table 2. The E_a of the defect presents around 300 K is 0.581 eV for the sample without Ge and 0.542 eV for the sample with 15 nm Ge, which is consistent with the value of Sn_{Zn} deep-donor state as reported in previous literatures [9,13]. It is worth mentioning that the Sn_{Zn} donor level is located near the midgap of CZTSSe material, therefore, it may act as the particularly harmful recombination center and the fatal killer for V_{oc} of CZTSSe solar cells. Furthermore, a smaller E_a is obtained after Ge incorporation, implying a faster carrier emission rate from the deep trap center [46,47]. More importantly, the density of Sn_{Zn} defects decrease from 8.97×10^{13} to 9.42×10^{12} cm^{-3}, which will effectively reduce the non-radiative recombination of charge carriers, leading to much higher V_{oc} and photovoltaic performance of CZTSSe solar cells. These results are well consistent with the $J-V$ features. Additionally, it is reported that there is a positive correlation between the intensity of the Raman modes located around 236 cm^{-1} and the density of detrimental [$2Cu_{Zn}$ + Sn_{Zn}] defect cluster [48]. As indicated in Fig. S4, the intensity of the Raman peak at ~236 cm^{-1} decreases as a result of 15 nm Ge-doping, which reflects the reduction of [$2Cu_{Zn}$ + Sn_{Zn}] defect cluster density. These are consistent well with the results of DLTS.

In order to study the effect of Ge doping on the carrier transport behaviors of the CZTSSe photovoltaic devices, EIS measurements were carried out on the reference and 15 nm Ge-containing devices. Fig. 7 presents the Nyquist plots of both devices under a bias of 0.45 V in the frequency range from 10^2 to 10^6 Hz under dark condition. From the well-established equivalent electrical circuit (inset of Fig. 7), the intercept of the x-axis corresponds to the series resistance (R_s), whereas the diameter of the half circle associates with the recombination resistance (R_j). The minority carrier lifetime τ can be calculated using the relationship of $\tau = R_j \times C$ [49], and the calculated parameters are listed in Table 3. It can be found that although the two devices exhibit almost the same value of R_s, however, after the introduction of Ge, the R_j of the photovoltaic

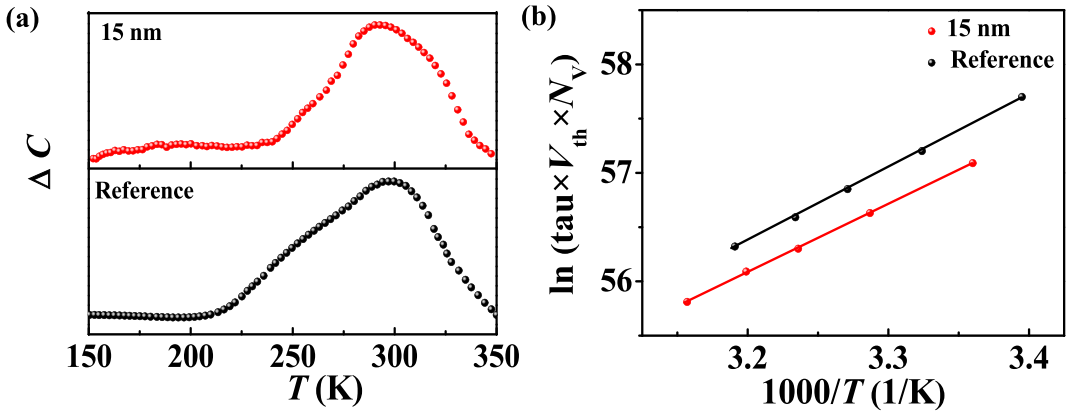

Fig. 6. (a) DLTS signal of Reference and 15 nm Ge samples. (b) Arrhenius plots corresponding to the peaks derived from DLTS spectra.

Table 2
Summary of the relevant parameters of Sn_{Zn} antisite defect for reference and 15 nm Ge samples.

Device	Peak Temp. (K)	E_a (eV)	N_T (cm^{-3})	Possible defect level
Reference	300	0.581	8.97×10^{13}	Sn_{Zn}
15 nm	298	0.542	9.42×10^{12}	Sn_{Zn}

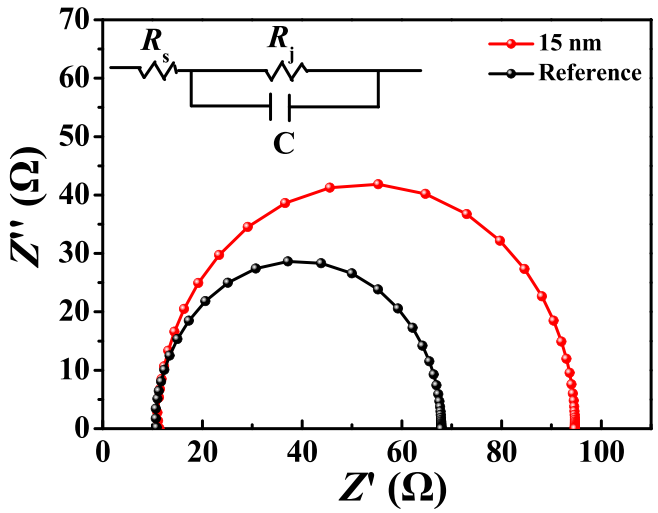

Fig. 7. Plots of Reference and 15 nm Ge samples under −0.45 V bias. Inset is the equivalent circuit.

Table 3
Summary of EIS of Reference and 15 nm Ge devices.

Device	R_s (Ω)	R_j (Ω)	C (nF)	τ (μs)
Reference	10.55	57.38	33.02	1.89
15 nm	10.96	83.79	31.67	2.65

device significantly increases from 57.38 to 83.79 Ω. The increased R_j for 15 nm Ge device indicates lower recombination rates [50], resulting in prolonged carrier lifetime from 1.89 to 2.65 μs. The enhanced recombination resistance may be ascribed to the decrease of recombination center arising from Sn_{Zn} deep traps, which is in good agreement with the DLTS results.

4. Conclusions

In summary, Ge was introduced into the kesterite semiconductors to passivate the active recombination centers in CZTSSe film. Meanwhile, it was observed that the crystalline quality of CZTSSe absorber layer was remarkably improved by Ge incorporating strategy. Consequently, the conversion efficiency of CZTSSe solar cells increased from 9.15% to 11.48%, largely attributing to the 41 mV V_{oc} enhancement. The combination of DLTS and EIS analysis revealed that the deep donor of Sn_{Zn} defects was suppressed thanks to Ge doping, resulting in reduction of recombination rate and prolonged carrier lifetime. These results provide direct evidence of tailoring deep traps in CZTSSe material through Ge implantation, which is of great importance for further identifying and assessing the main killer defects in kesterite-based photovoltaic materials, thereby removing the biggest barrier of large V_{oc} deficit for developing high efficient kesterite solar cells.

Declaration of Competing Interest

The authors declare that they have no known competing financial interests or personal relationships that could have appeared to influence the work reported in this paper.

Acknowledgments

This work was financially supported by the National Natural Science Foundation of China (U1904192, 62074052, 52072327, 61974173, 61874159 and 51802081), the Key Science and Technology Research Project of Education Department of Henan Province (19A140003), and the Key Science and Technology Program of Henan Province (192102210001), Zhongyuan Thousand Talents (Zhongyuan Scholars) Program of Henan Province (202101510004).

Appendix A. Supplementary data

Supplementary data to this article can be found online at https://doi.org/10.1016/j.jechem.2021.02.011.

References

[1] C. Yan, J. Huang, K. Sun, S. Johnston, Y. Zhang, H. Sun, A. Pu, M. He, F. Liu, K. Eder, L. Yang, J.M. Cairney, N.J. Ekins-Daukes, Z. Hameiri, J.A. Stride, S. Chen, M. A. Green, X. Hao, Nat. Energy 3 (2018) 764–772.
[2] M. Kumar, A. Dubey, N. Adhikari, S. Venkatesan, Q. Qiao, Energy Environ. Sci. 8 (2015) 3134–3159.
[3] H. Guo, G. Wang, R. Meng, Y. Sun, S. Wang, S. Zhang, J. Wu, L. Wu, G. Liang, H. Li, Y. Zhang, J. Mater. Chem. A 8 (2020) 22065–22074.
[4] W. Ki, H.W. Hillhouse, Adv. Energy Mater. 1 (2011) 732–735.
[5] B. Duan, L. Guo, Q. Yu, J. Shi, H. Wu, Y. Luo, D. Li, S. Wu, Z. Zheng, Q. Meng, J. Energy Chem. 40 (2020) 196–203.
[6] S. Bourdais, C. Choné, B. Delatouche, A. Jacob, G. Larramona, C. Moisan, Adv. Energy Mater. 6 (2016) 1502276.
[7] J.F. Guillemoles, T. Kirchartz, D. Cahen, U. Rau, Nat. Photon. 13 (2019) 501–505.
[8] D. Wang, W. Zhao, Y. Zhang, S. Liu, J. Energy Chem. 27 (2018) 1040–1053.
[9] A. Polizzotti, I.L. Repins, R. Noufi, S.H. Wei, D.B. Mitzi, Energy Environ. Sci. 6 (2013) 3171–3182.
[10] M.G. Gang, S.W. Shin, M.P. Suryawanshi, U.V. Ghorpade, Z.N. Song, J.S. Jang, J.H. Yun, H. Cheong, Y.F. Yan, J.H. Kim, J. Phys. Chem. Lett. 9 (2018) 4555–4561.
[11] T. Gokmen, O. Gunawan, T.K. Todorov, D.B. Mitzi, Appl. Phys. Lett. 103 (2013) 103506.
[12] S. Chen, A. Walsh, X.G. Gong, S.H. Wei, Adv. Mater. 25 (2013) 1522–1539.
[13] K. Nisika, M. Kaur, J. Kumar, Mater. Chem. A 8 (2020) 21547–21584.
[14] A. Walsh, S. Chen, S.H. Wei, X.G. Gong, Adv. Energy Mater. 2 (2012) 400–409.
[15] B. Duan, J. Shi, D. Li, Y. Luo, H. Wu, Q. Meng, Sci. China Mater. 63 (2020) 2371–2396.
[16] Z.K. Yuan, S. Chen, H. Xiang, X.G. Gong, A. Walsh, J.S. Park, I. Repins, S.H. Wei, Adv. Funct. Mater. 25 (2015) 6733–6743.
[17] Y.F. Qi, D.X. Kou, W.H. Zhou, Z.Z. Zhou, Q.W. Tian, Y.N. Meng, X.S. Liu, Z.L. Du, S. X. Wu, Energy Environ. Sci. 10 (2017) 2401–2410.
[18] T. Gershon, Y.S. Lee, P. Antunez, R. Mankad, S. Singh, D. Bishop, O. Gunawan, M. Hopstaken, R. Haight, Adv. Energy Mater. 10 (2016) 1502468.
[19] A. Guchhait, Z. Su, Y.F. Tay, S. Shukla, W. Li, S.W. Leow, J.M.R. Tan, S. Lie, O. Gunawan, L.H. Wong, ACS Energy Lett. 1 (2016) 1256–1261.
[20] Z. Su, J.M.R. Tan, X. Li, X. Zeng, S.K. Batabyal, L.H. Wong, Adv. Energy Mater. 5 (2015) 1500682.
[21] J. Fu, Q. Tian, Z. Zhou, D. Kou, Y. Meng, W. Zhou, S. Wu, Chem. Mater. 28 (2016) 5821–5828.
[22] C. Yan, K. Sun, J. Huang, S. Johnston, F. Liu, B.P. Veettil, K. Sun, A. Pu, F. Zhou, J.A. Stride, M.A. Green, X. Hao, ACS Energy Lett. 2 (2017) 930–936.
[23] J. Li, D. Wang, X. Li, Y. Zeng, Y. Zhang, Adv. Sci. 5 (2018) 170074.

[24] S. Ma, H. Li, J. Hong, H. Wang, X. Lu, Y. Chen, L. Sun, F. Yue, J.W. Tomm, J. Chu, S. Chen, J. Phys. Chem. Lett. 10 (2019) 7929–7936.
[25] J. Li, Y. Huang, J. Huang, G. Liang, Y. Zhang, G. Rey, F. Guo, Z. Su, H. Zhu, L. Cai, K. Sun, Y. Sun, F. Liu, S. Chen, X. Hao, Y. Mai, M.A. Green, Adv. Mater. 32 (2020) 2005268.
[26] J. Li, Z.K. Yuan, S. Chen, X.G. Gong, S.H. Wei, Chem. Mater. 31 (2019) 826–833.
[27] K. Biswas, S. Lany, A. Zunger, Appl. Phys. Lett. 96 (2010) 201902.
[28] G. Reya, G. Larramonab, S. Bourdaisb, C. Choinéb, B. Delatoucheb, A. Jacobb, G. Dennlerb, S. Siebentritt, Sol. Energy Mater. Sol. Cells 179 (2017) 142–151.
[29] S. Giraldo, E. Saucedo, M. Neuschitzer, F. Oliva, M. Placidi, X. Alcobe, V. Izquierdo-Roca, S. Kim, H. Tampo, H. Shibata, A. Pérez-Rodríguez, P. Pistor, Energy Environ. Sci. 11 (2018) 582–593.
[30] S. Giraldo, M. Neuschitzer, T. Thersleff, S. López-Marino, Y. Sánchez, H. Xie, M. Colina, M. Placidi, P. Pistor, V. Izquierdo-Roca, K. Leifer, A. Pérez-Rodríguez, E. Saucedo, Adv. Energy Mater. 5 (2015) 1501070.
[31] A. Crovetto, S. Kim, M. Fischer, N. Stenger, A. Walsh, I. Chorkendorff, P.K. Vesborg, Energy Environ. Sci. 13 (2020) 3489–3503.
[32] C. Yang, B. Zhou, S. Miao, C. Yang, B. Cai, W. Zhang, X. Xu, J. Am. Chem. Soc. 135 (2013) 5958–5961.
[33] S.Y. Kim, T.R. Rana, J.H. Kim, D.H. Son, K.J. Yang, J.K. Kang, D.H. Kim, Nano Energy 45 (2018) 75–83.
[34] R. Zhang, S.M. Szczepaniak, N.J. Carter, C.A. Handwerker, R. Agrawal, Chem. Mater. 27 (2015) 2114–2120.
[35] D.B. Khadka, S.Y. Kim, J.H. Kim, J. Phys. Chem. C 120 (2016) 4251–4258.
[36] Z. Zhang, Q. Gao, J. Guo, Y. Zhang, Y. Han, J. Ao, M.J. Jeng, F. Liu, W. Liu, Y. Zhang, Sol. RRL 4 (2020) 2000059.
[37] H. Xiao, W. Zhou, D. Kou, Z. Zhou, Y. Meng, Y. Qi, S. Yuan, Q. Tian, S. Wu, Green Chem. 22 (2020) 3597–3607.
[38] J. Guo, W. Zhou, Y. Pei, Q. Tian, D. Kou, Z. Zhou, Y. Meng, S. Wu, Sol. Energy Mater. Sol. Cells 155 (2016) 209–215.
[39] G. Brown, V. Faifer, A. Pudov, S. Anikeev, E. Bykov, M. Contreras, J. Wu, Appl. Phys. Lett. 96 (2010) 022104.
[40] J. Mattheis, P.J. Rostan, U. Rau, J.H. Werner, Sol. Energy Mater. Sol. Cells 91 (2007) 689–695.
[41] S. Giraldo, T. Thersleff, G. Larramona, M. Neuschitzer, P. Pistor, K. Leifer, A. Pérez-Rodríguez, C. Moisan, G. Dennler, E. Saucedo, Prog. Photovolt: Res. Appl. 24 (2016) 1359–1367.
[42] S. Kim, J.S. Park, A. Walsh, ACS Energy Lett. 3 (2018) 496–500.
[43] D. Xin, S. Tie, X. Zheng, J. Zhu, W.H. Zhang, J. Energy Chem. 46 (2020) 173–177.
[44] J.S. Park, S. Kim, Z. Xie, A. Walsh, Nat. Rev. Mat. 3 (2018) 194–210.
[45] S. Kim, J.A. Ḿarquez, T. Unold, A. Walsh, Energy Environ. Sci. 13 (2020) 1481–1491.
[46] H.S. Duan, W. Yang, B. Bob, C.J. Hsu, B. Lei, Y. Yang, Adv. Funct. Mater. 23 (2013) 1466–1471.
[47] X. Zhao, X. Chang, D. Kou, W. Zhou, Z. Zhou, Q. Tian, S. Yuan, Y. Qi, S. Wu, J. Energy Chem. 50 (2020) 9–15.
[48] Y. Sun, H. Guo, P. Qiu, S. Zhang, S. Wang, L. Wu, J. Ao, Y. Zhang, J. Energy Chem. 57 (2021) 618–626.
[49] Y.R. Lin, V. Tunuguntla, S.Y. Wei, W.C. Chen, D. Wong, C.H. Lai, L.K. Liu, L.C. Chen, K.H. Chen, Nano Energy 16 (2015) 438–445.
[50] D. Xin, S. Tie, R. Yuan, X. Zheng, J. Zhu, W.H. Zhang, ACS Appl. Mater. Interfaces 11 (2019) 44233–44240.